Petroleum Science 20 (2023) 1200–1216

Contents lists available at ScienceDirect

Petroleum Science

journal homepage: www.keaipublishing.com/en/journals/petroleum-science

Original Paper

Extraction of pipeline defect feature based on variational mode and optimal singular value decomposition

Min Zhang [a], Yan-Bao Guo [a, *], Zheng Zhang [a], Ren-Bi He [a, b], De-Guo Wang [a], Jin-Zhong Chen [b], Tie Yin [a, c]

[a] College of Mechanical and Transportation Engineering, China University of Petroleum, Beijing, 102249, China
[b] China Special Equipment Inspection and Research Institute, Beijing, 100029, China
[c] China Petroleum and Natural Gas Pipeline Research Institute Co. LTD, Langfang, Hebei 065000, China

ARTICLE INFO

Article history:
Received 21 August 2022
Received in revised form
2 November 2022
Accepted 4 November 2022
Available online 9 November 2022

Edited by Xiu-Qiu Peng

Keywords:
VMD method
VMK
SVD algorithm
Phase space matrix
Signal characteristics
Pipeline defect
Reconstruct

ABSTRACT

Because the magnetic signal information of pipeline defects obtained by magnetic flux leakage detection contains interference signals, it is difficult to accurately extract the features. Therefore, a novel pipeline defect feature extraction method based on VMD-OSVD (variational modal decomposition - optimal singular value decomposition) is proposed to promote the signal to noise ratio (SNR) and reduce aliasing in the frequency domain. By using the VMD method, the sampled magnetic signal is decomposed, and the optimal variational mode is selected according to the rate of relative change (VMK) of Shannon entropy (SE) to reconstruct the signal. After that, SVD algorithm is used to filter the reconstructed signal again, in which the H-matrix is optimized with the phase-space matrix to enhance SNR and decrease the frequency domain aliasing. The results show that the method has excellent denoising ability for defect magnetic signals, and SNR is increased by 21.01%, 24.04%, 0.96%, 32.14%, and 20.91%, respectively. The improved method has the best denoising effect on transverse mechanical scratches, but a poor denoising effect on spiral welding position. In the frequency domain, the characteristics of different defects are varied, and their corresponding frequency responses are spiral weld corrosion > transverse mechanical cracking > girth weld > deep hole > normal pipe. The high-frequency band is the spiral weld corrosion with $f_1 = 153.37$ Hz. The low-frequency band is normal with $f_2 = 1$ Hz. In general, the VMD-OSVD method is able to improve the SNR of the signal and characterize different pipe defects. And it has a certain guiding significance to the application of pipeline inspection in the field of safety in the future.

1. Introduction

The global oil and gas resources are abundant (Tong et al., 2018), but unevenly distributed. The reasonable allocation (Chen et al., 2020) of oil and gas resources is the top priority, and pipeline transportation is commonly used for oil and gas transportation on land and sea (Ge et al., 2020). However, the transportation environment is harsh. According to the statistics of the Pipeline and Hazardous Materials Safety Administration (PHMSA), the causes of oil and gas pipeline failure in the United.

States from 2010 to 2015 (Lam and Zhou, 2016) was that corrosion accounted for 25%, pipe body/weld material failure accounted for 22%, and excavation loss accounted for 15%, and so on. By the years, these statistics have increased each year. Therefore, the analysis of pipeline corrosion (Li et al., 2021a) and the exploration of defects in welds (Chaburkin, 1998) have become the focus of pipeline managers who have many pipeline inspection methods (Liu et al., 2021; Ghoni et al., 2014; Anon, 1998; Atzlesberger and Zagar, 2010; Coelho et al., 2018). Such as metal magnetic memory detection (Liu et al., 2021), eddy current detection (Ghoni et al., 2014), magnetic flux leakage (MFL) detection (Anon, 1998; Atzlesberger and Zagar, 2010; Coelho et al., 2018) and so on. MFL detection is a method to characterize pipe defects under saturated magnetic field by using the magnetic leakage intensity, which will be subject to fluctuations because of the equipment and environmental interference. As a result, it is essential to deal with the data of pipeline magnetic leakage intensity (Mukherjee et al., 2012), which provides a basis for the reliability analysis (Gu et al.,

* Corresponding author.
E-mail address: gyb@cup.edu.cn (Y.-B. Guo).

https://doi.org/10.1016/j.petsci.2022.11.007

2022) of pipelines. So, it is especially important to identify the characteristics of pipeline leakage signals.

Up to now, the magnetic signals of pipeline defects are divided into one-dimensional time series signals and image signals. Facing the image signal, Chen et al. (2014) and Prof. Yang (Yang et al., 2019a, 2019b) used a machine learning method to identify defective images. Huang et al. (2021) used the DEE method only for the crack images. Liu et al. (2020b) used the GCC-PHAT method for the water pipe defect localization. While the general sampling is obtained as a time series signal, wavelet denoising (WTD) and empirical modal denoising (EMD) are used to solve this signal interference problem. Han and Que (2006), Jachson et al. (2014) and Ghazali and Samta (2019) all used WTD method to achieve signal noise reduction processing and to improve the signal to noise ratio. Furthermore, in order to avoid the difficult problem of wavelet function selection, Cai (2006) and Chen et al. (2008) used EMD algorithm to effectively suppress the noise in the pipeline magnetic signal and to improve the robustness of the signal. Unfortunately, EMD algorithm is deficient in modal mixing and endpoint effects, which will affect the denoising ability of sampled signals. Variational modal decomposition (VMD) algorithm fills this gap, which is proposed by Pro. Dragomiretskiy in 2014 (Dragomiretskiy and Zosso, 2014) to filter adaptively the noisy signals. It is mainly applied to the signal denoising problem of rotating device defect detection. Just like, Wang, An and Pan, Lian, Li and others have adopted VMD algorithm to solve the bearing, gear and another dynamic equipment signal of interference problems. Wang et al. (2015) verified the superiority of VMD algorithm by comparing four signal processing methods of gas turbine vibration signals, including VMD, EWT, EEMD and EMD. An and Pan (2017) proposed the component information after VMD decomposition of wind turbine bearing vibration signals with permutation entropy as the index and then used the nearest neighbor algorithm to identify bearing faults. Lian et al. (2018) and Li et al. (2019) combined with other algorithms to solve the adaptive problem of VMD algorithm, overcome the excessive decomposition of the signal, and effectively identify the vibration source in the measured signal. While we face the problem of pipeline static equipment interference, Lu et al. (2021), Wang et al. (2022) and Zhou et al. (2022) have improved the signal-to-noise ratio of the detected acoustic signals with the help of VMD algorithm and verified the effectiveness of the method. Unlike the acoustic signal, the magnetic signal is a low frequency sensitive signal. When using VMD algorithm to process magnetic signals, the reconstructed signal processing has the problem of frequency domain aliasing.

In order to overcome the above problems, this paper proposes a pipeline defect feature extraction method based on variational modal decomposition-optimal singular value decomposition (VMD-OSVD). The method improves the signal-to-noise ratio (SNR) of defective magnetic signals and characterizes the pipeline of defective magnetic signals. The main work of this paper is as follows: first, the sampled magnetic signal is decomposed by VMD, and the optimal variational mode is selected according to the rate of relative change (VMK) of Shannon entropy (SE) to reconstruct the signal. Then, the reconstructed signal is filtered again by using the SVD algorithm, and the H-matrix is optimized with the phase-space matrix to enhance SNR and decrease the frequency domain aliasing to characterize the frequency domain features of the defect. The results show that the proposed method has better denoising ability for defective magnetic signals, having all raised the SNR, and obtaining characteristics of different pipeline defects in the frequency domain. In a word, it provides an engineering reference value for data feature extraction in pipeline inspection engineering.

2. Signal feature extraction theory of VMD-OSVD algorithm

VMD-OSVD algorithm based on the leakage detection method is proposed, and the flowchart is shown in Fig. 1. In Fig. 1, the improved algorithm is introduced in the dashed box. Compared with the VMD algorithm, it can improve the SNR in the time domain and characterize different pipeline defects in the frequency domain. The first step of the process is the input of the signal, in which the MFL intensity signal sampled from pipeline defects is input. Next, in the second step, the signal is processed by the VMD algorithm (Dragomiretskiy and Zosso, 2014), which improves the adaptive selection problem of the VMD algorithm by the principle rate of relative change (VMK) of SE (Shannon, 1948; Yol et al., 2018; Vashishtha and Kumar, 2022), and the optimal order is determined, as the light orange block in Fig. 1 shows the VMD algorithm by the principle rate of relative change (VMK) of Shannon entropy. Further, in the third step, the signal is processed by OSVD algorithm, in which the phase space method (Buzug and Pfister, 1992; Jiang et al., 2020) is used to improve the H-matrix (Zhao and Ye, 2009; Li et al., 2021; Golafshan and Sanliturk, 2016) in SVD algorithm to avoid the problem of mixing in the signal frequency domain, as the light blue block in Fig. 1 shows the improvement of the matrix in SVD algorithm by using the phase space method. And in the fourth step, the SVD feature components are selected to reconstruct the signal according to the difference spectrum. Moreover, in the fifth step, the reconstructed signal is envelope demodulated. Eventually, in the sixth step, the frequency domain features of the signal are extracted to characterize the defect features, and the output is the spectral features of the sampled signal in the frequency domain conditions after VMD-OSVD processing.

The theoretical study of the VMD-OSVD algorithm mainly contains the adaptive selection of the VMD and the optimization improvement of the SVD, which further improves SNR of the magnetic signal. Finally, the reconstructed signal is analyzed in time spectrum. The method improves the frequency domain mixing problem in the VMD algorithm and fills the gap in the field of frequency domain analysis of pipeline magnetic signals.

2.1. VMD algorithm

VMD technique, proposed by Pro. Dragomiretskiy in 2014 (Dragomiretskiy and Zosso, 2014), is an adaptive modal variational signal processing method that uses sub-signals with different frequency domains to be superimposed. For detection signals with interference, the high frequency noise signal is removed through modal decomposition, and the reasonable sub-signal frequency is selected to reflect the defect features of the detection signal.

2.1.1. VMD fundamental theory

The VMD analysis method is based on the time domain decomposition of the signal $H_p(t)$, which is calculated as follows:

$$\min_{\{u_m,\omega_m\}}\left\{\sum_m\left\|\partial_t[\delta(t)+j/\pi t)*u_m(t)]e^{-j\omega_m t}\right\|_2^2\right\} \quad s.t.\sum_{m=1}^{M}u_m=H_p(t) \tag{1}$$

In Eq. (1), M is the modal order number ($M = 3$–7); m is each IMF component; $\{u_m\}$ is the modal component; $\{\omega_m\}$ is the central frequency; $\delta(t)$ is Dirac function; {*} is a convolutional operator.

The Lagrange multiplier operator $\lambda(t)$ and penalty factor α are brought to solve the variational problem. And the frequency domain updates of estimated $\{u_m\}$, $\{\omega_m\}$ and $\lambda(t)$ are computed as follows.

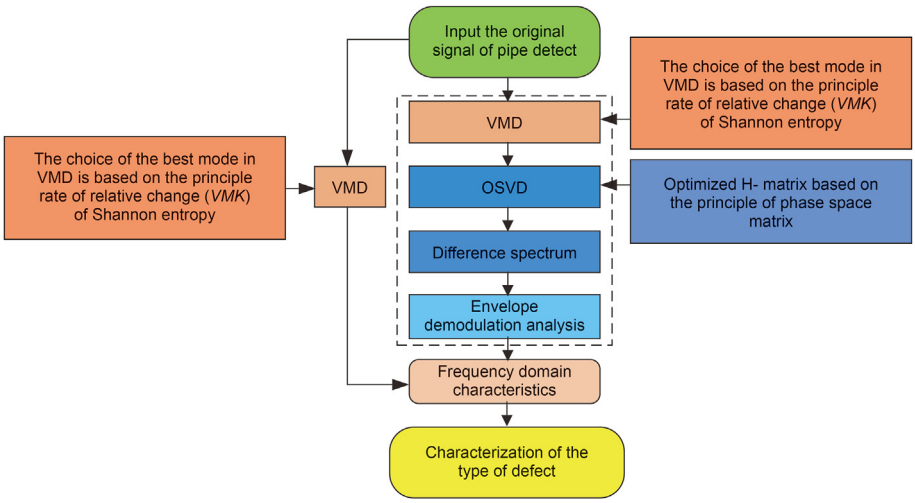

Fig. 1. Flowchart of VMD-OSVD algorithm.

$$\widehat{u}_m^{n+1}(\omega)=\frac{\widehat{f}(\omega)-\sum_{i\neq m}\widehat{u}_i(\omega)+\frac{\widehat{\lambda}(\omega)}{2}}{1+2\alpha(\omega-\omega_m)^2} \tag{2}$$

$$\omega_m^{n+1}=\frac{\int_0^\infty \omega\left|\widehat{u}_m^{n+1}(\omega)\right|^2 \mathrm{d}\omega}{\int_0^\infty \left|\widehat{u}_m^{n+1}(\omega)\right|^2 \mathrm{d}\omega} \tag{3}$$

$$\widehat{\lambda}^{n+1}(\omega)=\widehat{\lambda}^{n}(\omega)+\gamma\left(\widehat{f}(\omega)-\sum_m \widehat{u}_m^{n+1}(\omega)\right) \tag{4}$$

Among them, γ is the update factor; n is the number of iterations; $\widehat{u}_m^{n+1}(\omega)$, $\widehat{u}_i(\omega)$, $\widehat{f}(\omega)$, $\widehat{\lambda}(\omega)$ is the result of the Fourier transform, respectively.

2.1.2. Determination of mode for VMD

The VMD method is used to reduce the noise of the pipeline magnetic signal with different modal components. So, it is necessary to select the most suitable noise reduction order and modal components. Using Eqs. (1)–(4), the parameters of the VMD algorithm are designed to complete the noise reduction process for the different orders [$M = 3, 4, 5, 6, 7$]. An index parameter is designed to select the mode component, namely Shannon entropy (Shannon, 1948), and to calculate the defect information of different components under each mode successively, whose expression is:

$$R(u)=-\sum_{t=1}^{N} p(H_p(t))\log(p(H_p(t))) \tag{5}$$

where $p(H_p(t))$ represents the degree of uncertainty of the pipeline inspection system; N represents the signal length; u is the total IMF component per mode. The index of SE is often used in the field of pipeline safety. The larger the SE value, the more white noise in the signal. Or vice versa. Hence, SE value can be used to characterize the noise-denoising effect and extract the best VMD filtering output.

The SE value is the basis for determining the mode of the VMD. On this basis, an objective algorithm, which is named VMK, is proposed for the adaptive selection of the variational mode. Where the expression of VMK equation is calculated as follows:

$$VMK_m=\sum_{u}^{m-1}\frac{R(u)-R(u+1)}{R(u+1)} \tag{6}$$

In Eq. (6), VMK_m is calculated to obtain the best mode. When the VMK_m is minimum, the M_0 is the best VMD mode. Therefore, the principle rate of relative change (VMK) of SE is used to determine the optimal mode component, so as to obtain pure signals easily.

2.2. OSVD algorithm

The VMD algorithm completes the noise reduction process for the sampled signal. The time-frequency domain characteristics of the optimal mode M_0 are analyzed, and it is found that the frequency domain part of the signal overlapped. To solve this problem, the OSVD method is proposed for the secondary processing of the magnetic signal to improve SNR of the signal, and to modify the signal frequency-domain aliasing problem, and establish the frequency spectrum to discriminate the defect characteristics.

2.2.1. SVD fundamental theory

There is a set of signals $H_p(t)=[H_p(1),H_p(2),\ldots,H_p(N)]$ that have been processed by VMD. Then, it can be reconstructed by filtering of the OSVD. The Hankel matrix of the signal in the OSVD can be established based on the signal reconstruction theory (Kalman, 1996; Wang, 2015c; Golafshan and Sanliturk, 2016). The theory also solves the problem of fracture density and orientation in petroleum geology (Li et al., 2021b). And this matrix H (Zhao and Ye, 2009; Liu et al., 2015c; Golafshan and Sanliturk, 2016) is as follows:

$$H=\begin{bmatrix} H_p(1) & H_p(2) & \cdots & H_p(q) \\ H_p(2) & H_p(3) & \cdots & H_p(q+1) \\ \vdots & \vdots & \cdots & \vdots \\ H_p(p) & H_p(p+1) & \cdots & H_p(N) \end{bmatrix}, \tag{7}$$

$$1<q\leq p<N, p+q-1=N$$

In which, Matrix H reveals the abrupt dynamic characteristics of the noisy signal by reconstructing the eigenvalues of the suborbital matrix. The signal can therefore be characterized as $H = D + W$. Where matrix D denotes the smooth signal. Matrix W represents

the noisy signal.

Then, the matrix H is decomposed by selecting valid singular values. And the decomposition of the Hankel matrix can be obtained as follows.

$$\begin{cases} H = UGV^T = V\begin{bmatrix} \sum & 0 \\ 0 & 0 \end{bmatrix} V^{\mathrm{T}} \\ U \times U^{\mathrm{T}} = I_q, V \times V^{\mathrm{T}} = I_p \end{cases} \tag{8}$$

In Eq. (8), U is matrix of entries of $q \times q$. V^T is matrix of entries of $p \times p$. And G is a diagonal matrix of $q \times p$, the main diagonal elements are $q = n - p + 1$, namely:

$$\sum = \begin{bmatrix} diag(\sigma_1, \sigma_2, \cdots, \sigma_\tau) \\ O \end{bmatrix}, \tau = \min(q, p) \tag{9}$$

where $\sum = diag(\sigma_1, \sigma_2, \cdots, \sigma_\tau)$ are the singular values of matrix H, and whose elements on the diagonal are arranged in descending order, just like $\sigma_1 \geq \sigma_2 \geq \cdots \geq \sigma_\tau$, then τ is the rank of the attractor orbit matrix.

Next, selecting component signals is the key to separating noise. The concept of singular value difference spectrum is introduced to select component signals. The calculation formula is as follows:

$$z_k = \sigma_k - \sigma_{k+1}, k = 1, 2, \ldots, q-1 \tag{10}$$

In which, the difference spectrum is the sequence formed by $z = (z_1, z_2, \cdots, z_{q-1})$, which reflects the variation trend of two adjacent singular values. If the singular value decreases greatly at the serial number k, a peak value will appear in the difference spectrum, and there must be the maximum peak z_k among many peaks. However, the singular value serial number k is the maximum mutation point, which is also the demarcation point between pure signal and noise signal. So, only the first k components are selected for superposition, which can reduce noise interference and achieve the purpose of noise reduction and feature extraction.

2.2.2. Frequency domain characteristics of reconstructed signals

According to the difference spectrum, singular eigenvalues are selected to reconstruct signal $S(t)$. Then, the reconstructed envelope spectrum is used for the reconstructed characterization, the expression of which is

$$S(t) = U\sum V^T = \left(u_1 \hat{\sigma}_1 v_1^T + u_2 \hat{\sigma}_2 v_2^T\right) \tag{11}$$

$$h[S(t)] = \frac{1}{\pi} \int_{-\infty}^{+\infty} \frac{s(\overrightarrow{\tau})}{t - \overrightarrow{\tau}} d\overrightarrow{\tau} = S(t) * \frac{1}{\pi t} \tag{12}$$

$$o(t) = S(t) + jh[S(t)] \tag{13}$$

$$Bl(t) = \sqrt{S^2(t) + h^2[S(t)]} \tag{14}$$

where $h[S(t)]$ is the Hilbert signal of reconstructed signal within two of time intervals $\overrightarrow{\tau}$. $o(t)$ is the analytic signal of reconstructed signal $S(t)$ and Hilbert signal $h[S(t)]$. $Bl(t)$ is the envelope signal after taking the mode of the analytic signal $o(t)$.

2.2.3. Reconstruction of optimal H-matrix based on phase space method

Constructing H-matrix is the core problem of SVD algorithm. The variation of matrix dimension affects the accuracy of quadratic denoising. To improve the H-matrix of SVD algorithm, the phase space matrix (Buzug and Pfister, 1992; Jiang et al., 2020) is proposed in this paper. Therefore, the H′-matrix is first established as

$$\begin{aligned} \mathrm{H}' &= f\left(H_p(t)\right) = H_p(t + \psi) \\ &= \left(H_p(t), H_p(t + \psi) \ldots, H_p(t + (\chi - 1)\psi)\right), \\ & 1 \leq t \leq t + (\chi - 1)\psi \end{aligned} \tag{15}$$

where χ is the embedding dimension and ψ is the delay time. The appropriate phase space matrix H′ is obtained by adjusting the delay time and embedding dimension.

3. Pipeline MFL signal processing and analysis

Based on the magnetic dipole model, the mathematical model of MFL detection in pipeline is established to verify the effectiveness of the pipeline defect feature identification method. Taking the rectangular defect as an example, it is assumed that the rectangular defect has a width of $2a$, and the depth d. The magnetic charge density on the two sides of the defect is σ_s, with equal magnitude and opposite sign. There is no magnetic charge distribution at the defect mouth and other parts. The pipeline defect of MFL signal is obtained from Eq. (16).

$$\begin{cases} H_p(x) = 2\sigma_s \cdot \left[\arctan\left(\dfrac{d(x-a)}{(x+a)^2 + y(y+d)}\right) - \arctan\left(\dfrac{d(x-a)}{(x-a)^2 + y(y+d)}\right)\right] \\ H_p(y) = \sigma_s \cdot \ln\left(\dfrac{\left[(x+a)^2 + \left(y + d^2\right)\right] \times \left[(x-a)^2 + y^2\right]}{\left[(x-a)^2 + \left(y + d^2\right)\right] \times \left[(x-a)^2 + y^2\right]}\right) \end{cases} \tag{16}$$

In which, $H_p(x)$ and $H_p(y)$ are the axial component and radial component of the pipe leakage detection respectively; (x, y) is the coordinates of the probe; σ_s is the surface density of magnetic charge, and its calculation formula:

$$\sigma_s = \frac{2.65}{2\pi} \times \frac{\frac{d}{2a} + 1}{\frac{1}{\mu_0} * \left(\frac{d}{2a} + 1\right)} H_a \tag{17}$$

where H_a is the strength of the application of the magnetic field. So, the above mathematical Eqs. (16) and (17) are edited through the Matlab platform, and the given values of its parameters are shown in Table 1:

Therefore, according to Table 1, the parameters of mathematical

Table 1
Reference table for parameter values.

Parameter	Symbol	Parameter values
Mileage	x	[-0.1, 0.1] m
Probe lift off value	y	0.001 m
The width of the defect	a	[0.002, 0.016] m
The depth of the defect	d	[0, 0.006] m
Vacuum permeability	μ_0	$4\pi \times 10^{-7}$
Sample interval in depth	Δ_1	0.0001 m
Sample interval in length	Δ_2	0.0002 m

model simulation are designed. While keeping the lift value parameter unchanged, the defect size is changed, which includes the research process of changing the defect depth d and width a. The results are shown in figure Fig. 2. Fig. 2(a) shows the variation of magnetic field strength of the defect depth d, in which the abscissa represents the mileage and the ordinate represents the magnetic leakage field strength. Fig. 2(b) shows the variation of magnetic leakage field strength with defect width a.

According to Fig. 2, we can find that the magnetic leakage field strength of the defect changes with the depth d and width a of the defect. Fig. 2(a) shows that, when the defect width a is unchanged, only the defect depth d is changed. With the increase of defect depth d, the strength of axial magnetic field decreases gradually. As can be seen in Fig. 2(b), with the defect depth d unchanged, the magnetic field intensity at the defect gradually increases with the change of the defect width a, and the value of the abscissa corresponding to the peak and valley value of the magnetic field intensity curve increases again.

3.1. Statement of the relative rates of change in VMK_m

Any set of data is selected for the argument of the algorithm in this paper. Therefore, we choose the data set with $d = 3$ mm in Fig. 2(a) and add a set of Gaussian noise to complete the algorithm argument. The data expression at this point is.

$$B = H_p(y) + W\left(\rho, \zeta^2\right) \tag{18}$$

Where ρ, ζ is the expectation and variance of the Gaussian distribution, respectively.

The SE of each IMF component is calculated using Eq. (5). And the VMK for various modes is calculated by Eq. (6). Thus, the relative rates of change of SE and VMK for various modes are shown in Fig. 3, in which the abscissa represents modal order number and the ordinate represents SE and the rate of relative change (VMK).

From Fig. 3, it can be seen that the optimal order of the mode is determined by VMK_m, which has the smallest entropy coefficient and also indicates the low white noise content of the defect leakage

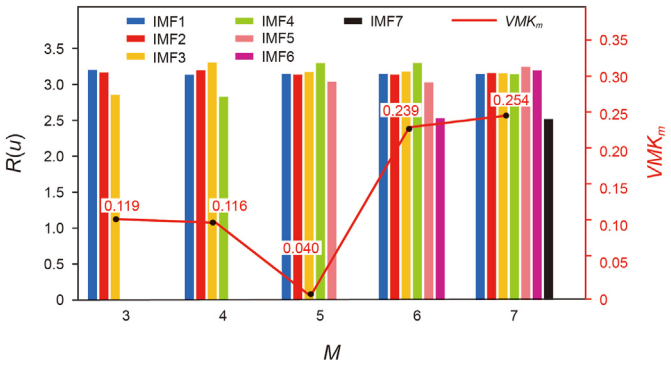

Fig. 3. Calculation results of SE and the rate of relative change (VMK). IMF1 is represented as the first mode component. IMF2 represents the second mode component. IMF3 represents the third mode component. IMF4 is the fourth mode component. IMF5 shows the fifth mode component. IMF6 is shown as the sixth mode component. IMF7 is the seventh mode component.

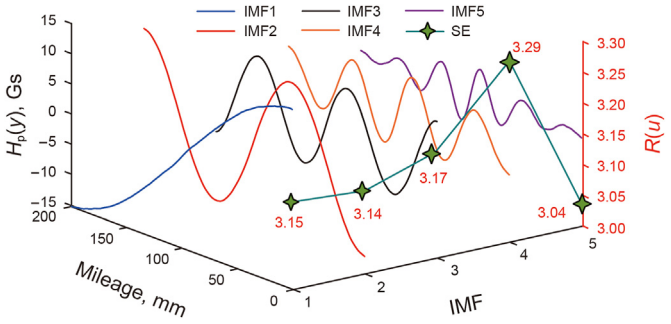

Fig. 4. Different modal components and SE values of the MFL signal. IMF1 is represented as the first mode component. IMF2 represents the second mode component. IMF3 represents the third mode component. IMF4 is the fourth mode component. IMF5 shows the fifth mode component. The dark green line shows the entropy result for each component.

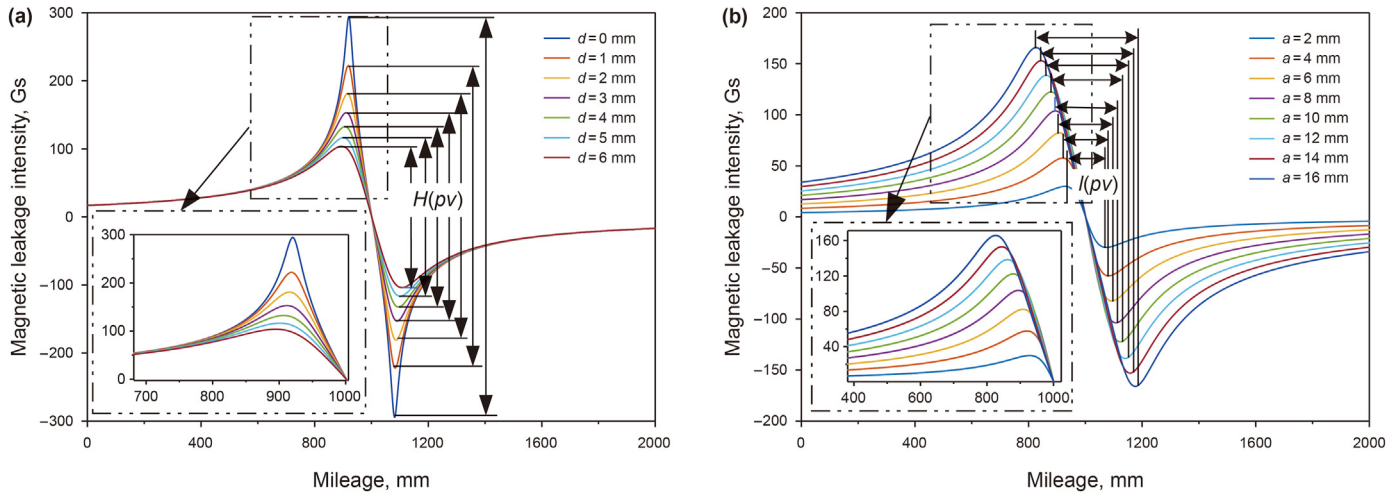

Fig. 2. Numerical simulation curve of leakage magnetic field of pipeline defects. (**a**) Variation relationship of magnetic field intensity of pipeline defects under different defect depth d; (**b**)variation relationship of magnetic field intensity of pipeline defects under different width a.

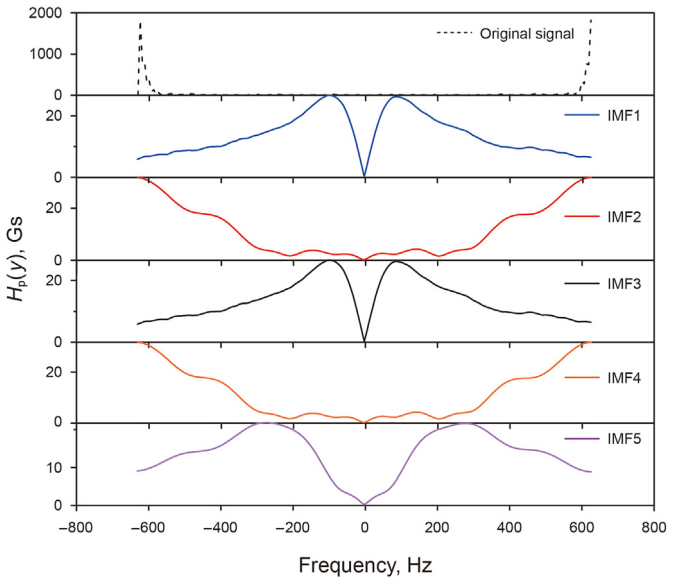

Fig. 5. The frequency domain results of the variational mode with $M = 5$. Original signal is represented as the original signal of the pipeline test data sample. IMF1 is expressed as the first mode component signal after VMD algorithm processing. IMF2 is denoted as the second mode component signal after VMD algorithm processing. IMF3 is indicated as the third mode component signal after VMD algorithm processing. IMF4 is presented as the fourth mode component signal after VMD algorithm processing. IMF5 is displayed as the fifth mode component signal after VMD algorithm processing.

magnetic field signal. Therefore, the minimum $VMK_m = 0.040$, and the corresponding optimal number of modal components is $M_0 = 5$. Further, the modal component of each order of the VMD optimal mode of $M_0 = 5$ is output, as follows in Fig. 4. The horizontal coordinate is mileage. And H_y is magnetic leakage intensity. IMF is the modal component of each order of the VMD optimal mode.

According to the minimum SE in Fig. 4, the high information degree of the pipeline leakage field is IMF5, which $R(u = 5) = 3.04$. In this way, it is chosen as the original signal for OSVD secondary noise reduction. Meanwhile, the output frequency response results corresponding to the time domain features of different components are shown in Fig. 5.

According to Fig. 5, it is easy to see that aliasing occurs in the frequency domain. In order to avoid overlapping phenomena in frequency domain, OSVD reconstruction is applied to the data to alleviate this problem.

3.2. Demonstrating the effectiveness of the OSVD method

To demonstrate the effectiveness of the OSVD method, the H-matrix of the method is firstly established. The H′-matrix of OSVD is established by the phase space matrix. Secondly, OSVD secondary denoising is utilized to complete signal feature extraction, time-domain reconstruction, frequency domain analysis, and so on, avoiding the problem of frequency-domain aliasing. Finally, the eigenvalue of the signal is employed as the signal identification scalar to distinguish the signal.

3.2.1. Phase space construction

During the construction, phase space structure is mainly applied. There are two general choices for the delay time, which are linear autocorrelation and parallel mutual information. We have finished performing operations on both. An optimal matrix construction result is chosen according to the SE and SNR. For embedding dimension determination, there are three methods to determine the embedding size containing the geometric invariance method, the pseudo-nearest point method, and the modified method of the pseudo-nearest point method. The best-constructed matrix is obtained by crossover experiments with results in Table 2.

In this work, the SNR and SE are used to select the best constructed H-matrix. With the principle of maximum SNR and minimum SE, the most suitable H′-matrix can be obtained from Table 2. The chosen H′-matrix is the dimension m of the phase matrix obtained by Liapunov and the time ψ of the phase matrix gained by autocorrelation, whose SNR is 10.5498 and SE is 2.9922. H′-matrix is optimized by phase space matrix as shown in Fig. 6, which it represents expanding the dimension of H′- matrix.

According to the results of the phase space matrix in Fig. 6, one-dimensional data can be constructed into multidimensional data through phase space matrix, and the best is three-dimensional data, whose matrix is [3 × 187]. Plotting the curve shows that the best representation of the signal is the signal changes in a similar pattern to the one-dimensional data, but the signal is still mixed with some disturbances. At the same time, in the frequency domain feature extraction process, there is still the aforementioned problem of frequency-domain aliasing. Therefore, OSVD secondary denoising of the signal is crucial.

3.2.2. Frequency domain characteristics of reconstructed signals

The phase space matrix is exploited to construct H′-matrix, and then the eigenvector extraction of the OSVD and the subsequent time-frequency domain spectrum analysis are completed. The rank order of singular decomposition is vital. The difference spectrum of

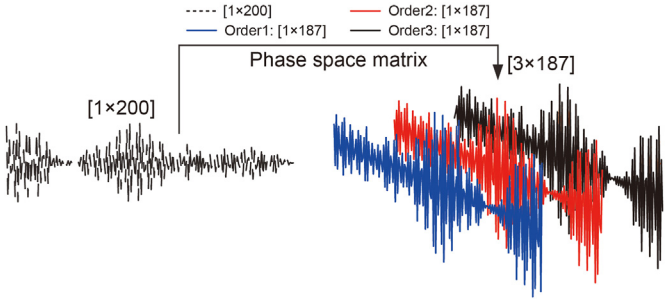

Fig. 6. H′-matrix in phase space construction. The dashed line represents the reconstructed signal of VMD, and the scale is [1 × 200]. The blue line indicates the signal of the first order after the phase space matrix up-dimensioning, and the scale is [1 × 187]. The red line represents denotes the signal of the second order after the phase space matrix up-dimensioning, and the scale is [1 × 187]. The black line represents the third order after the phase space matrix up-dimensioning, and the scale is [1 × 187]. Therefore, these three lines form the new H′-matrix after dimensionality enhancement.

Table 2
Phase space parameter crossover experimental index results.

Indicators	Autocorrelation			Mutual information		
	Lyapunov to get dimensions	The cao function retrieves the dimension	Correlation dimension to obtain the dimension	Lyapunov to get dimensions	The cao function retrieves the dimension	Correlation dimension to obtain the dimension
SNR	10.5498	6.7332	10.1565	5.6229	8.0462	5.9872
SE	2.9922	2.9847	2.9909	2.9704	2.9603	2.9702

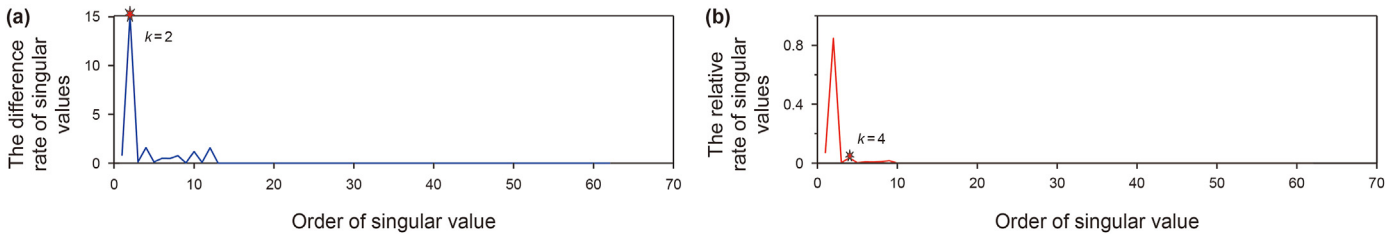

Fig. 7. Effective rank order of signal SVD reconstruction. (**a**) The order is determined by the unilateral wave difference spectrum method, as shown in the blue line. (**b**) The order is determined by the difference between unilateral maximum, as shown in the red line.

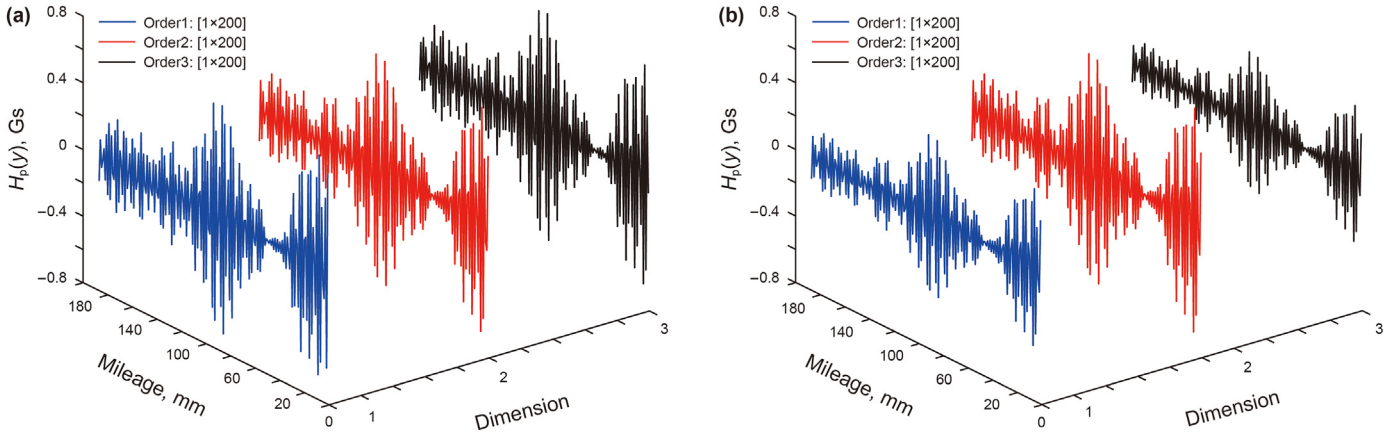

Fig. 8. The time-domain waveform of signal OSVD reconstruction. (**a**) The time-domain waveform determined by the unilateral wave difference spectrum method. The blue line represents the first order signal in the time domain determined by the unilateral wave difference spectrum method, and the scale is [1 × 200]. The red line indicates the second-order signal in the time domain determined by the unilateral wave difference spectrum method, in which the scale is [1 × 200]. The black line represents the third-order signal in the time domain determined by the unilateral wave difference spectrum method, in which the scale is [1 × 200]. (**b**) The time-domain waveform is determined by the difference between unilateral maximum. The blue line represents the first order signal in the time domain determined by the difference between unilateral maximum, which the scale is [1 × 200]. The red line indicates the second-order signal in the time domain determined by the difference between unilateral maximum, which the scale is [1 × 200]. The black line represents the third-order signal in the time domain determined by the difference between unilateral maximum, which the scale is [1 × 200].

the singular value eigenvalues is calculated according to Eq. (10). The effective reconstruction order is determined using the one-sided fluctuation principle and the one-sided maximum value principle, so the effective order results are shown in Fig. 7.

As shown in Fig. 7(a), the differential spectral order of $k = 2$ is determined using the one-sided fluctuation principle. The differential spectral order of $k = 4$ is identified using the one-sided fluctuation principle, as shown in Fig. 7(b). Further, OSVD reconstruction is carried out on the signals on the basis of the effective rank order. The reconstruction results are shown in Fig. 8.

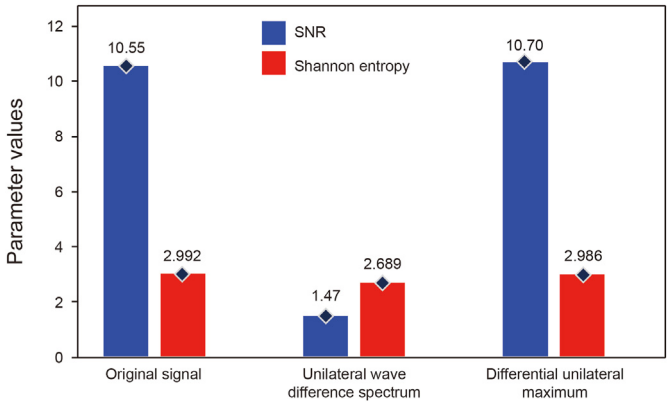

Fig. 9. Change value of index coefficient after signal reconstruction. Blue block is the SNR result, red block is the Shannon entropy result.

As can be seen from Fig. 8(a), after signal reconstruction, the waveform shape of the signal is similar to that of the original signal, but the amplitude of the signal is too small, which filters out the amplitude modulation characteristics of the original signal, resulting in the reduction of over-noise.

And Fig. 8(b) shows that the waveform shape is consistent with the trend of the original signal, and the amplitude of the signal is similar. Intuitively, the noise reduction effect is satisfactory. Therefore, the signal reconstructed by the differential spectrum method and unilateral maximum value method is selected for index analysis, as shown in Fig. 9.

It can be seen from the SNR and SE from Fig. 9 that the signal reconstructed by differential unilateral maximum method improves the SNR, and SNR = 10.70. Meanwhile, the SE is within the error tolerance, and the variation difference is almost negligible. So, the feasibility of this method and the effectiveness of the reconstructed signal are again demonstrated. Compared with the original signal, the SNR is improved by 1.40% and the SE is slightly lost by 0.20%.

In addition, the frequency domain curve and envelope spectrum curve of the reconstructed signal are analyzed as shown in Fig. 10. It can be seen that the waveform does not appear spectrum aliasing phenomenon in the signal frequency domain. Simultaneously, multiple frequency domain peaks appear around $f_3 = 613$ Hz in FFT frequency domain, which can represent the characteristics of the original signal. And multiple frequency peaks appear at frequency $f_1 = 25$ Hz in the envelope spectrum of the reconstructed signal, which lays a foundation for time-spectrum analysis of signals.

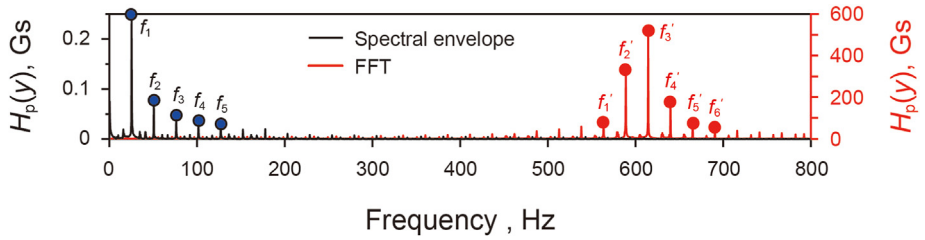

Fig. 10. Frequency domain characteristics after signal reconstruction. The black line is the spectral envelope processing result, and the red line is the FFT spectrum processing result.

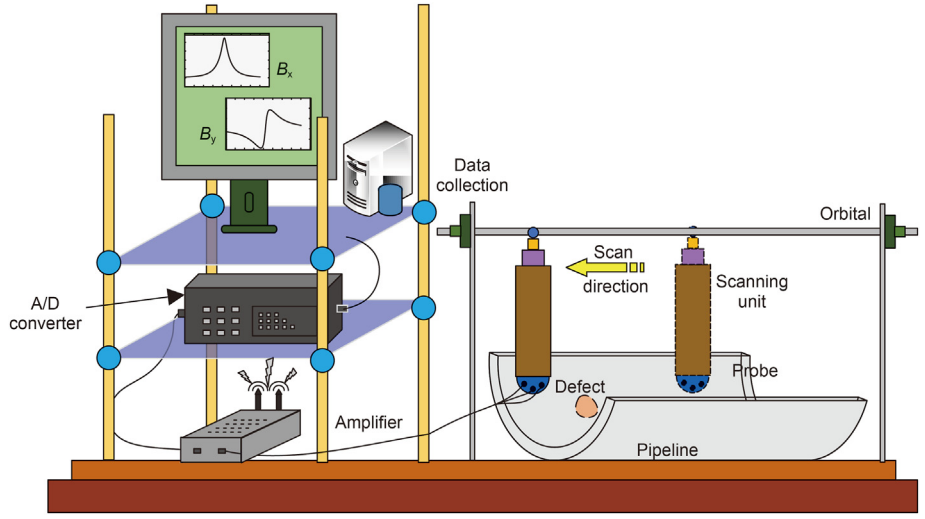

Fig. 11. Pipeline defect magnetic flux leakage laboratory test platform.

In summary, the VMD-OSVD algorithm is used to improve the SNR of time-domain signals while solving the mixing problem of the frequency domain signal in this article. Thus, the algorithm compensates for the characteristic characterization of the magnetic signal in the frequency domain.

4. Experiment analysis

Based on the above research, a dual-axis MFL detection device is designed in the laboratory, which is shown in Fig. 11. It is a real-time internal detection device with a scanning speed of 6 m/s. It includes a data acquisition unit, scanning unit, power supply, data acquisition card, upper computer acquisition interface, A/D converter, probes and pipe. In this case, the individual probes use Hall elements type SS49E and are placed perpendicular to each other to detect leakage magnetic fields in different axes. The power supply is 1600 W. The data acquisition card has a maximum of 18 channels and a maximum sampling frequency of 450 kHz. When a pipe is detected, one probe is arranged circumferentially to complete the pipe detection and move in the axial direction. The probes collect a one-dimensional time-series signal.

4.1. Time-frequency domain analysis of sampled signals

In the laboratory, we tested five samples of data, including pipe in the normal, ring weld, pits, spiral weld corrosion, and transverse mechanical cracking. Each test sample is completed through 72 channels, respectively. And the data results are shown in Fig. 12.

According to Fig. 12, the signal is messy in the time domain with a large noise. The signals are almost identical in the frequency domain with $f = 1$ Hz, which is difficult to distinguish. Therefore, MFL signals of pipeline defects need to be denoised in the time domain and reduced aliasing in the frequency domain. Firstly, VMD algorithm is used for signal denoising. Further, according to the formula of SE index parameters in Eq. (5), the optimal VMD denoising mode as M_0 is determined. So, the results are shown in Fig. 13.

As can be seen from Fig. 13, the SEs in each IMF component of different denoising mode of the VMD algorithm are calculated for these five defect samples. According to the principle of minimum VMK_m, the best denoising mode M_0 is selected for the five different defect samples, as shown in the curves for the different defect samples in Fig. 13. Therefore, in Fig. 13(a) of the normal signal, it is found that $M_0 = 4$ is best denoising mode. From Fig. 13(b), we know that $M_0 = 7$ is best denoising mode in the girth weld. Via Fig. 13(c), $M_0 = 6$ is the optimal denoising mode for corrosion at spiral weld. After Fig. 13(d), the optimal denoising mode for transverse mechanical scratches is the same as for spiral welds with $M_0 = 6$. According to Fig. 13(e), we know that $M_0 = 6$ is best denoising mode in the dent.

Further, we need to investigate the optimal components for different denoising orders for different defects. The choice of the optimal composition is based on the calculation of SE in Eq. (5). Taking the minimum entropy as the selection principle, the best component is selected on merit. The time-domain characteristics of different components and SE are shown in Fig. 14.

Fig. 14 shows the different IMF components and the corresponding SE values for the optimal mode of five defects. According to the principle of minimum SE, the optimal IMF components is selected. In Fig. 14(a), the minimum SE value of the normal signal corresponds to the component IMF1 with the SE value of $R_n(u = 1) = 2.86$, so this component can be used as the original signal for the

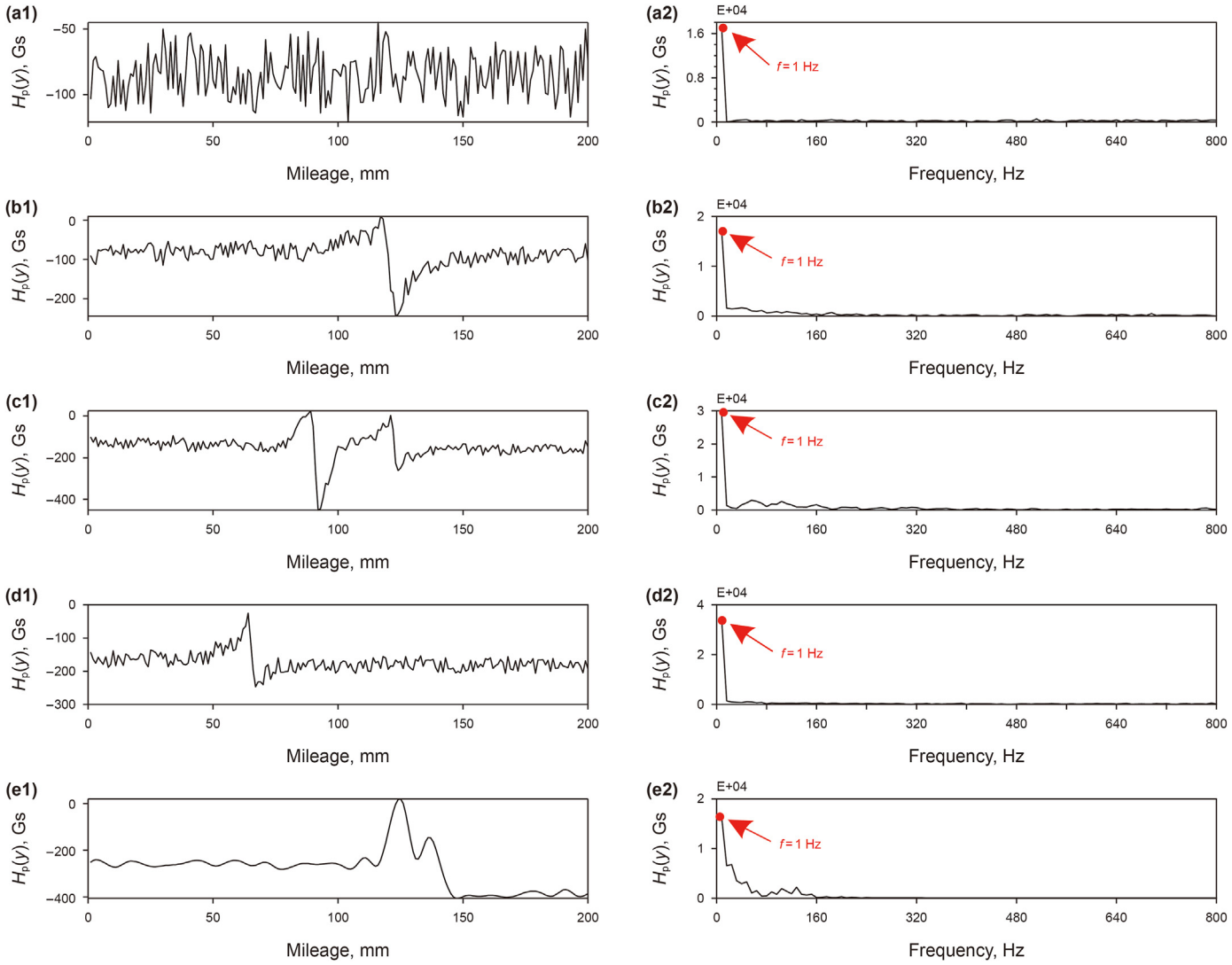

Fig. 12. Time-frequency domain curve characteristics of acquired signal for pipeline defect detection. (a-1) is the time domain curve characteristics of an acquired signal under the normal state of the pipeline. (a-2) is the frequency domain curve characteristics of the acquired signal for the normal pipeline. (b-1) is the time domain curve characteristics of the acquired signal under girth-welding position. (b-2) is the frequency domain curve characteristics of the acquired signal for girth-welding position. (c-1) is the time domain curve characteristics of the acquired signal under corrosion at spiral welding position. (c-2) is the frequency domain curve characteristics of acquired signal for corrosion at spiral welding position. (d-1) is the time domain curve characteristics of the acquired signal under transverse mechanical scratches. (d-2) is the frequency domain curve characteristics of the acquired signal for transverse mechanical scratches. (e−1) is the time domain curve characteristics of the acquired signal under dent. (e−2) is the frequency domain curve characteristics of acquired signal for dent.

secondary noise reduction. Similarly, via Fig. 14(b), the optimal component of girth-welding position denoising is IMF3 with the SE value $R_g(u = 3) = 2.36$; By Fig. 14(c), the best component of the corrosion at spiral welding position denoising is IMF6 with the SE value $R_s(u = 6) = 2.24$; It is found that the best component of transverse mechanical scratches denoising is IMF4 with the SE value $R_t(u = 4) = 2.02$ in Fig. 14(d); It is known that the optimal component of dent is IMF3 with the SE value $R_d(u = 3) = 2.55$ in Fig. 14(e).

The optimal modal component is selected by the minimum SE value, and the signal component is further characterized in the frequency domain to observe whether there is the spectrum aliasing problem. Then, the results are shown in Fig. 15.

According to the frequency domain characteristics of different components of the optimal modal order in Fig. 15, it can be seen that there is no aliasing phenomenon in the frequency domain except IMF ($u = 1$) component, and aliasing problem exists in other mode components IMF(u) to a certain extent. Therefore, the frequency domain feature extraction of the five defects cannot be completed. The frequency domain confusion is not conducive to analyzing the frequency domain characteristics of the signal, and the extraction of the frequency domain representations of different defects cannot be completed. In order to solve the above frequency domain overlap problem, OSVD secondary denoising of the signal is needed to further complete the frequency domain characterization of different types of pipe defects.

4.2. Frequency domain characterization of OSVD

From Fig. 15, there is an aliasing problem in the frequency domain of different defects, so it is necessary to perform enhanced time domain denoising for different signals. According to the optimal value selection results of the optimal components in Fig. 14, modal components with different defects are selected

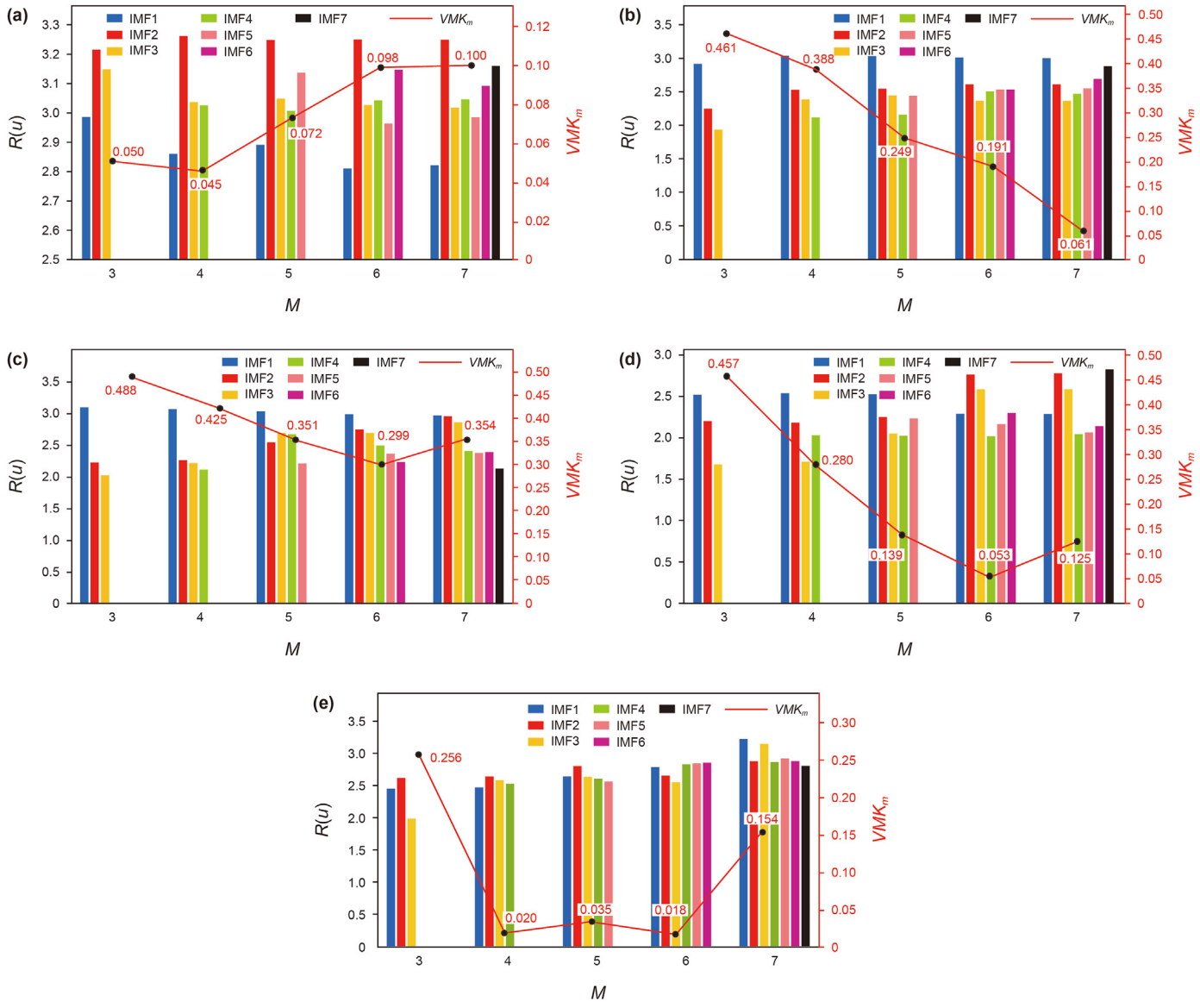

Fig. 13. Calculation results of SE and the rate of relative change (VMK) for five defects. IMF1 is represented as the first mode component. IMF2 represents the second mode component. IMF3 represents the third mode component. IMF4 is the fourth mode component. IMF5 shows the fifth mode component. IMF6 is shown as the sixth mode component. IMF7 is the seventh mode component. Red line is the rate of relative change (VMK). (**a**) Calculation results of SE and VMK in normal state of pipeline. (**b**) Calculation results of SE and VMK under girth-welding position. (**c**) Calculation results of SE and VMK under corrosion at spiral welding position. (**d**) Calculation results of SE and VMK under transverse mechanical scratches. (**e**) Calculation results of SE and VMK under dent.

to complete OSVD secondary denoising of signals. Firstly, referring to the phase space combination model in Table 2, the optimal component completes the construction of the phase space H′-matrix. Then, the constructed H′-matrix is used to perform secondary denoising of OSVD. Finally, the envelope spectrum and FFT frequency domain of denoised signals after reconstruction are analyzed to complete the characterization of different defects in the frequency domain.

4.2.1. Construction of phase space H′-matrix

According to Eq. (15), the phase space matrices of different defect signals are obtained to complete the construction of the H′-matrix of OSVD. The result is shown below in Fig. 16.

It can be seen from Fig. 16 that the signal of the improved H′-matrix is similar to the original signal. To a certain extent, the time-domain characteristics of the best component signal IMF are expressed, which lays the foundation for the signal to complete the feature vector extraction for OSVD and the subsequent time-frequency domain analysis.

4.2.2. OSVD reconstruction

The constructed H′-matrix is subjected to OSVD reconstruction and feature extraction in frequency domain. The waveform shape of the signal reconstructed by OSVD is consistent with the trend of the H′-matrix signal, and the amplitudes are comparable, which shows a good noise reduction effect intuitively. The reconstructed curves are shown in Fig. 17.

By comparing Figs. 16 and 17, it can be seen that the amplitude and variation rule of the signal is not changed before and after OSVD algorithm processing. Meanwhile, by comparing the SNR and SE index coefficient, it can be seen that the processed signal is better, the noise in the signal is small, and the curve is smooth.

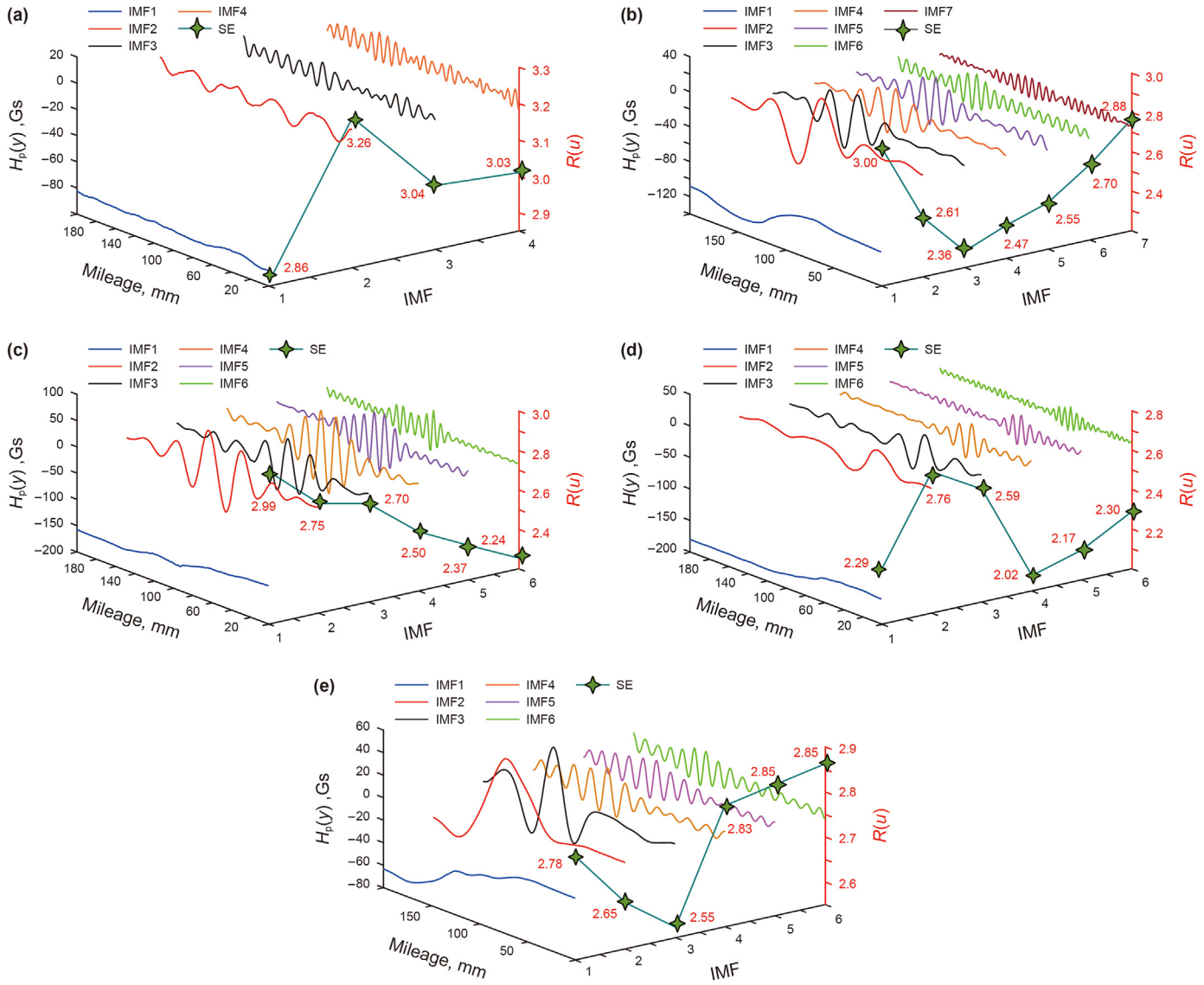

Fig. 14. Different modal components and entropy values for five defects. IMF1 is represented as the first mode component. IMF2 represents the second mode component. IMF3 represents the third mode component. IMF4 is the fourth mode component. IMF5 shows the fifth mode component. IMF6 is shown as the sixth mode component. IMF7 is the seventh mode component. The dark green line shows the entropy result for each component. (a) Different modal components and entropy values for normal; (b) Different modal components and entropy values for the girth-welding position; (c) Different modal components and entropy values for corrosion at spiral welding position; (d) Different modal components and entropy values for transverse mechanical scratches; (e) Different modal components and entropy values for dent.

By comparing the index coefficients from Fig. 18, it shows that the signal before and after reconstruction not only improves the SNR, but also reduces the SE. For the normal in Fig. 18(a), the SNR increases by 21.01%, and the SE decreases by 1.39%; The position signal of ring welding reconstructed from Fig. 18(b) shows the SNR is from 18.58 to 24.46 and the SE is from 2.39 to 2.42, with a slight increase of 1.24% in the SE; For the signal for corrosion at spiral welding position in Fig. 18(c), the SNR is raised by 0.96%; Via Fig. 18(d), the SNR of the transverse mechanical scratches signal reconstructed is from 11.40 to 16.80 and the SE is from 2.06 to 1.99; From Fig. 18(e), the SNR of reconstructed dent signal is enhanced by 20.91%, and the SE is declined by 0.39%.

4.2.3. Frequency domain characterization

Based on the parameter of the index coefficient, the denoising advantage after signal reconstruction is demonstrated. The reconstructed signal can better characterize the frequency domain characteristics of different defect types and can visually characterize different defects, which is a new method to characterize pipeline defects. Therefore, the frequency domain analysis results of the reconstructed signal are shown in Fig. 19.

As can be seen from Fig. 19, the frequency domain results of the five defects can visually identify the features of different defects, solving the problem of frequency-domain mixing in Fig. 12. It becomes a new method for extracting MFL signals. Fig. 19 (a) shows that it is difficult to extract the FFT frequency domain characteristics of normal signals with $f'_1 = 1$ Hz, and in the envelope spectrum, the frequency of normal signals with $f_1 = 25.39$ Hz that shows the decaying trend.

From Fig. 19 (b), it can be seen that the features in frequency domain of the girth-welding position can be characterized by the peak and sub-peak with the FFT frequency values of $f'_3 = 51.19$ Hz and $f'_2 = 25.39$ Hz, respectively. And the sub-peak appears to the left of the peak. At the same time, the corresponding envelope spectrum tends to decay after $f_1 = 25.8$ Hz.

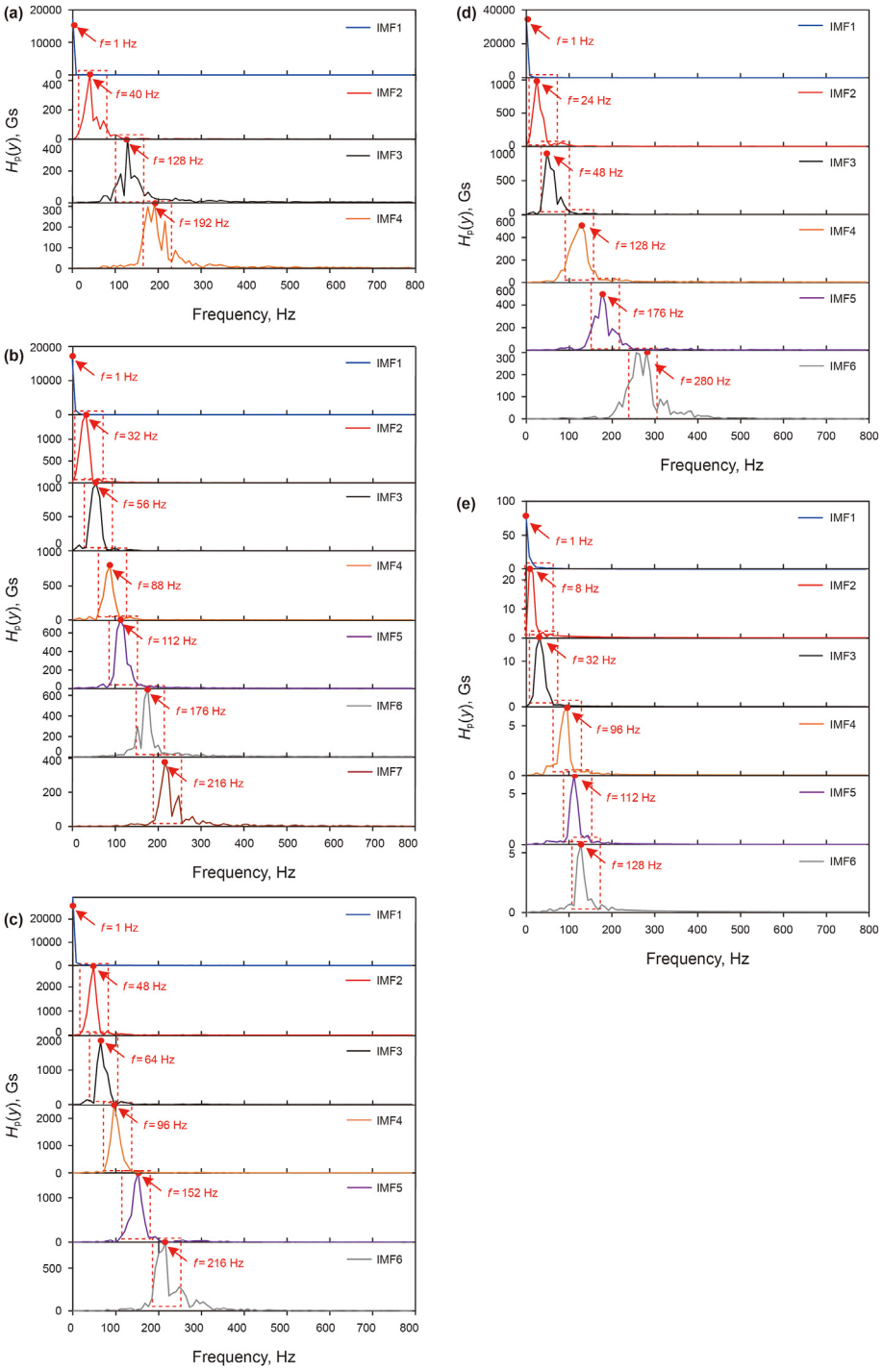

Fig. 15. Frequency domain characteristics of different modal components of five defects. IMF1 is represented as the frequency domain characteristic signal of the first mode component. IMF2 represents the frequency domain characteristic signal of the second mode component. IMF3 represents the frequency domain characteristic signal of the third mode component. IMF4 is the frequency domain characteristic signal of the fourth mode component. IMF5 shows the frequency domain characteristic signal of the fifth mode component. IMF6 is shown as the frequency domain characteristic signal of the sixth mode component. IMF7 is the frequency domain characteristic signal displayed as the seventh mode component. (**a**) Frequency domain characteristics of different modal components for normal. (**b**) Frequency domain characteristics of different modal components for girth-welding position. (**c**) Frequency domain characteristics of different modal components for corrosion at spiral welding position. (**d**) Frequency domain characteristics of different modal components for transverse mechanical scratches. (**e**) Frequency domain characteristics of different modal components for dent.

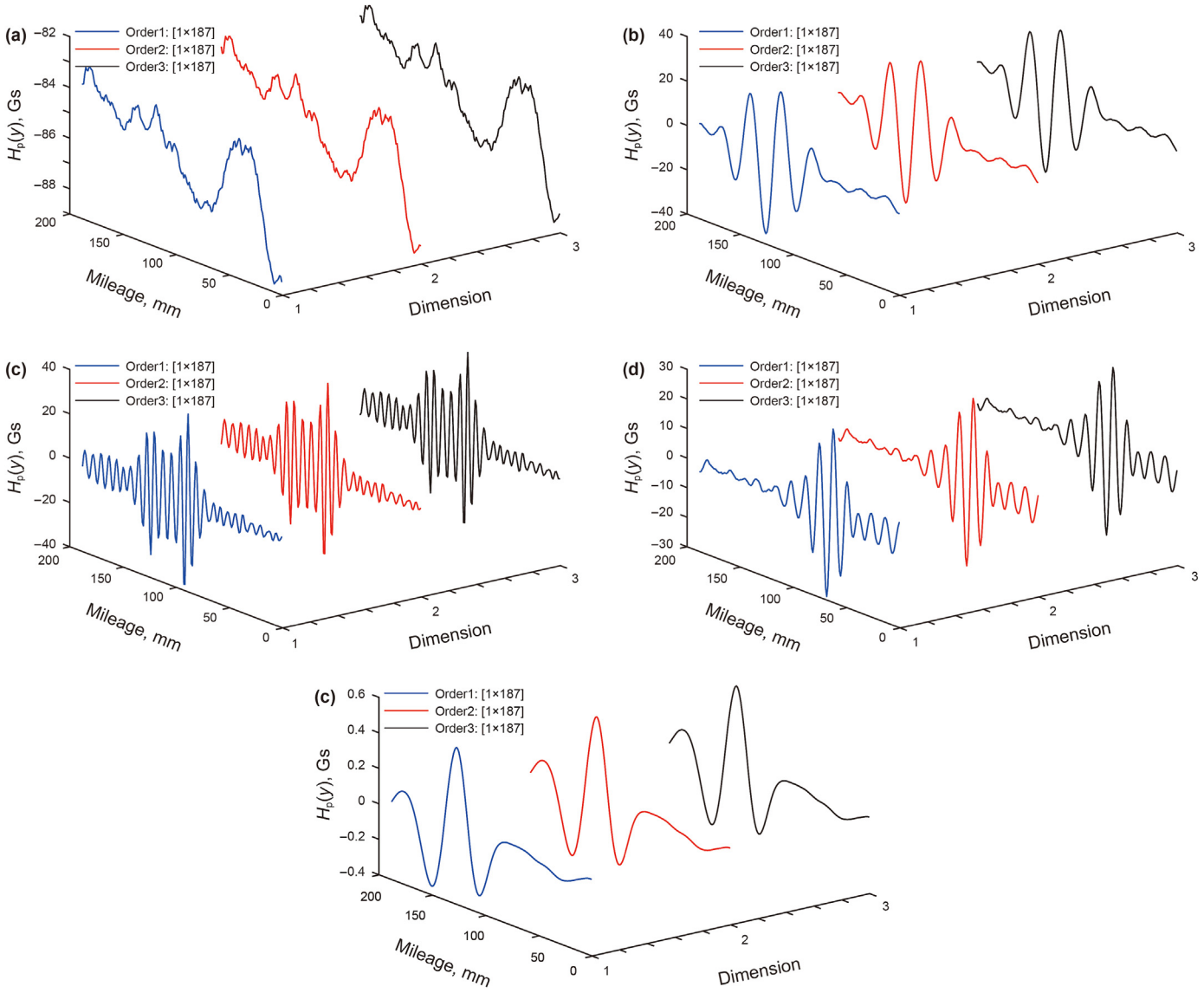

Fig. 16. Phase space H′-matrix for five defects. The blue line indicates the signal of the first order after the phase space matrix up-dimensioning, and the scale is [1 × 187]. The red line represents denotes the signal of the second order after the phase space matrix up-dimensioning, and the scale is [1 × 187]. The black line represents the third order after the phase space matrix up-dimensioning, and the scale is [1 × 187]. Therefore, these three lines form the new H′ matrix after dimensionality enhancement. (**a**) Phase space H′-matrix for normal; (**b**) Phase space H′-matrix for girth-welding position; (**c**) Phase space H′-matrix for corrosion at spiral welding position; (**d**) Phase space H′-matrix for transverse mechanical scratches; (**e**) Phase space H′-matrix for dent.

In the same way, the corrosion defect of the corrosion at spiral welding position is characterized in Fig. 19 (c), with the corresponding sub-peak and peak FFT frequency occurring at $f'_4 = 128.17$ Hz and $f'_3 = 153.57$ Hz, respectively. And the sub-peak appears to the right of the peak. However, at $f'_7 = 390.48$ Hz, a second peak appears in the FFT frequency domain. There are also two peaks in the corresponding envelope spectrum, located at $f_1 = 25.39$ Hz and $f_7 = 262.5$ Hz, respectively.

As can be seen in Fig. 19 (d), the frequency domain profile of the transverse mechanical scratches increases and then decreases, with a maximum at the peak $f'_5 = 102.38$ Hz, which in turn can be used to characterize it. And the frequency domain curve of the envelope spectrum changes in the same trend, with maximum peak at $f_2 = 25.39$ Hz and then followed by decreasing trend thereafter.

The dent is characterized by the corresponding frequency domain features as shown in Fig. 19 (e), which gradually decreases in the frequency domain spectrum past $f'_2 = 25.40$ Hz, and the influence of the sub-peak is small. In the envelope spectrum, the maximum frequency is $f_2 = 25.7$ Hz, which is consistent with the change of the frequency domain curve.

In short, the five kinds of defects are almost different peak frequencies in the frequency domain spectrum. However, when the girth-welding position and corrosion at spiral welding position are represented in the envelope spectrum, the peak value in the frequency domain is similar, so the sub-peak can be used for secondary representation to avoid the problem of unclear representation. Unlike the time-domain characterization of the magnetic signal of the pipeline defect, Peng and Kercel (Kercel et al., 2003; Peng et al., 2020) is mainly based on the waveform variation characteristics of the time-domain signal characterization, the waveform similarity cannot be distinguished and the secondary hazard caused by the defect cannot be assessed. Therefore, the characterization of pipeline frequency domain curves, making up for the lack of time-frequency domain signals, is a new defect

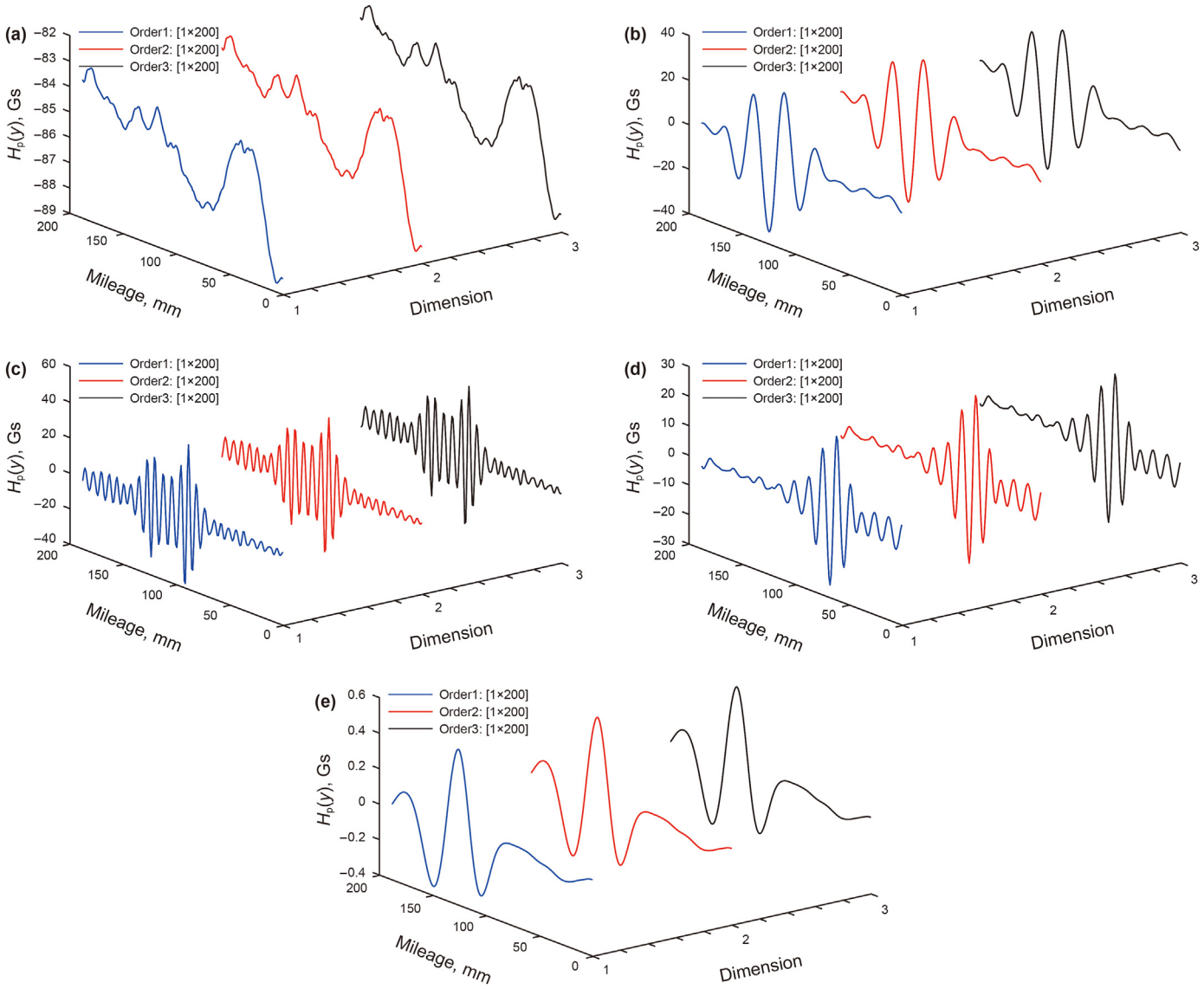

Fig. 17. OSVD reconstructed time-domain signal of the five defects. The blue line represents the first order signal in the time domain, and the scale is [1 × 200]. The red line indicates the second-order signal in the time domain, and the scale is [1 × 200]. The black line represents the third-order signal in the time domain, and the scale is [1 × 200]. (**a**) Reconstructed time domain signal for normal; (**b**) Reconstructed time domain signal for girth-welding position; (**c**) Reconstructed time domain signal for corrosion at spiral welding position; (**d**) Reconstructed time domain signal for transverse mechanical scratches; (**e**) Reconstructed time domain signal for dent.

characterization method to provide application value for pipeline safety, which also demonstrates the effectiveness of the pipeline defect signal characterization method proposed in this paper.

5. Conclusion

The magnetic signals of pipeline defects mainly show time-domain characteristics and their signal curves change in similar forms, so it is difficult to distinguish. In addition, there are fewer methods to characterize them in the frequency domain. Consequently, it aggravates the difficulty factor of pipeline signal characterization in time-frequency domain. In this paper, a new method based on VMD-OSVD is proposed to characterize the magnetic signals of pipeline defects in time-frequency domain. In the time domain, the SNR of the defect magnetic signal is improved. In the frequency domain, the frequency response represents different characteristics of pipeline defects. All in all, it lays the foundation for pipeline safety engineering.

(1) Aiming at the problem of difficult identification of pipeline defect signals, VMD denoising is used for modal decomposition processing, and the principle of minimizing the relative rate of change (VMK) of SE is proposed to select the variational mode M_0, so the signal is reconstructed. Furthermore, the OSVD algorithm is put forward to reconstruct the defect signal. The phase space matrix is modified to improve the H′-matrix of SVD model to reconstruct the defect signal and effectively characterize the type of pipeline defect in the frequency domain.
(2) The VMD-OSVD method improves the SNR in the time domain. The MFL signals of the five kinds of pipeline defects include normal, girth-welding position, corrosion at spiral

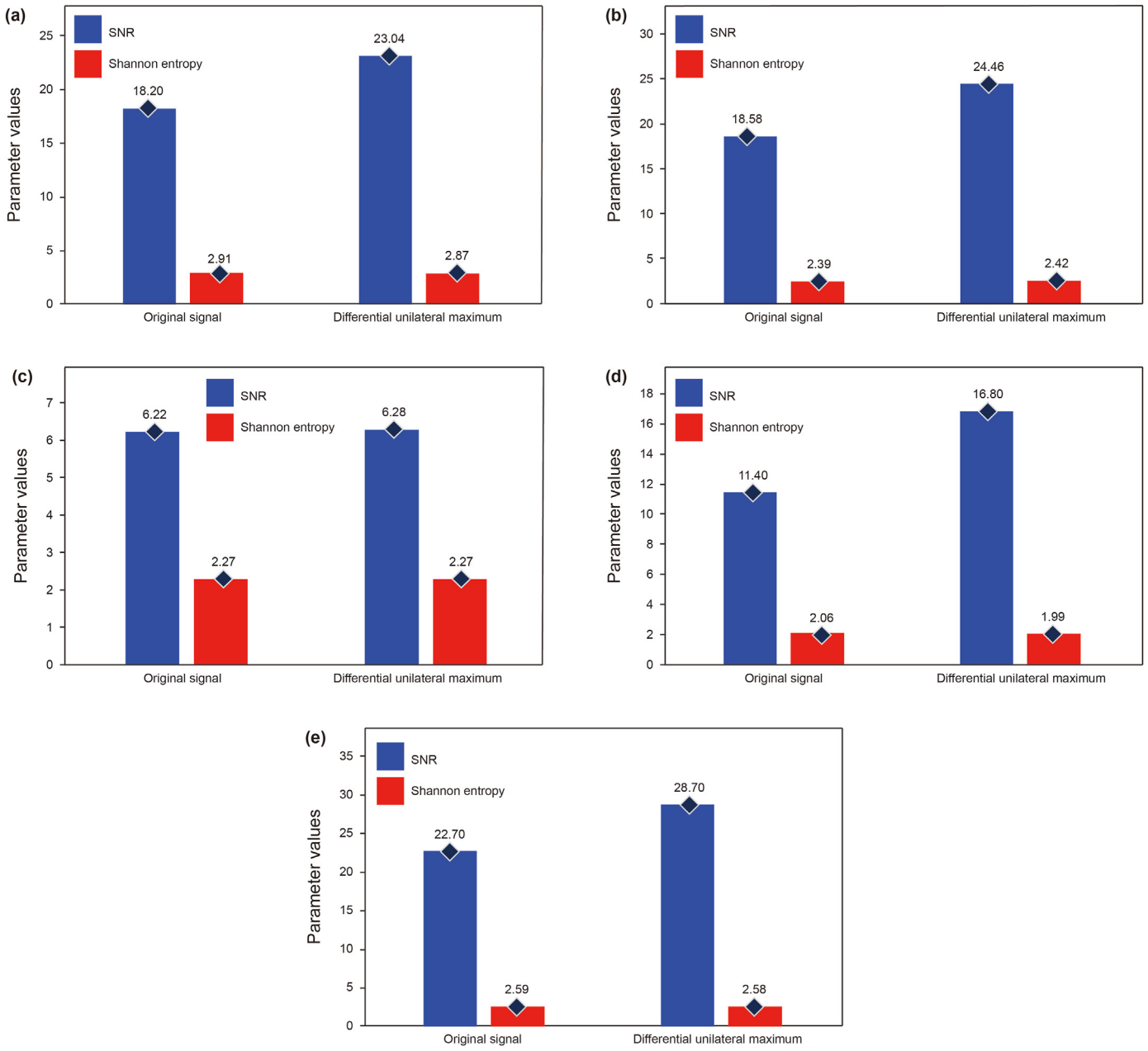

Fig. 18. Index coefficients of the five defects after signal reconstruction. Blue is the SNR result, red is the Shannon entropy result. (**a**) SNR and SE for normal; (**b**) SNR and SE for girth-welding position; (**c**) SNR and SE for corrosion at spiral welding position; (**d**) SNR and SE for transverse mechanical scratches; (**e**) SNR and SE for dent.

welding position, transverse mechanical scratches, and dent, whose SNR increased by 21.01%, 24.04%, 0.96%, 32.14%, and 20.91%. The improved method has the best denoising effect on transverse mechanical scratches, but a poor denoising effect on spiral welding position.

(3) In the frequency domain, based on the FFT frequency domain characterization of the five kinds of pipeline defects by the VMD-OSVD algorithm, the corresponding frequency responses are ranked from high to low frequency as follows in corrosion at spiral welding position > transverse mechanical scratches > girth-welding position > dent > normal pipe. The high-frequency band is spiral weld corrosion with a frequency response of $f_1^{'} = 153.37$ Hz. The low-frequency band is a normal pipe with a frequency response of $f_2^{'} = 1$ Hz. In this way, it will help future researchers to identify the signals of different defects.

(4) VMD-OSVD method can improve the SNR in the time domain, and characterize different pipeline defects in the frequency domain. Although the data solved so far is limited, the exploration of multiple defects will not stop. Therefore, it will play an important role in pipeline safety evaluation.

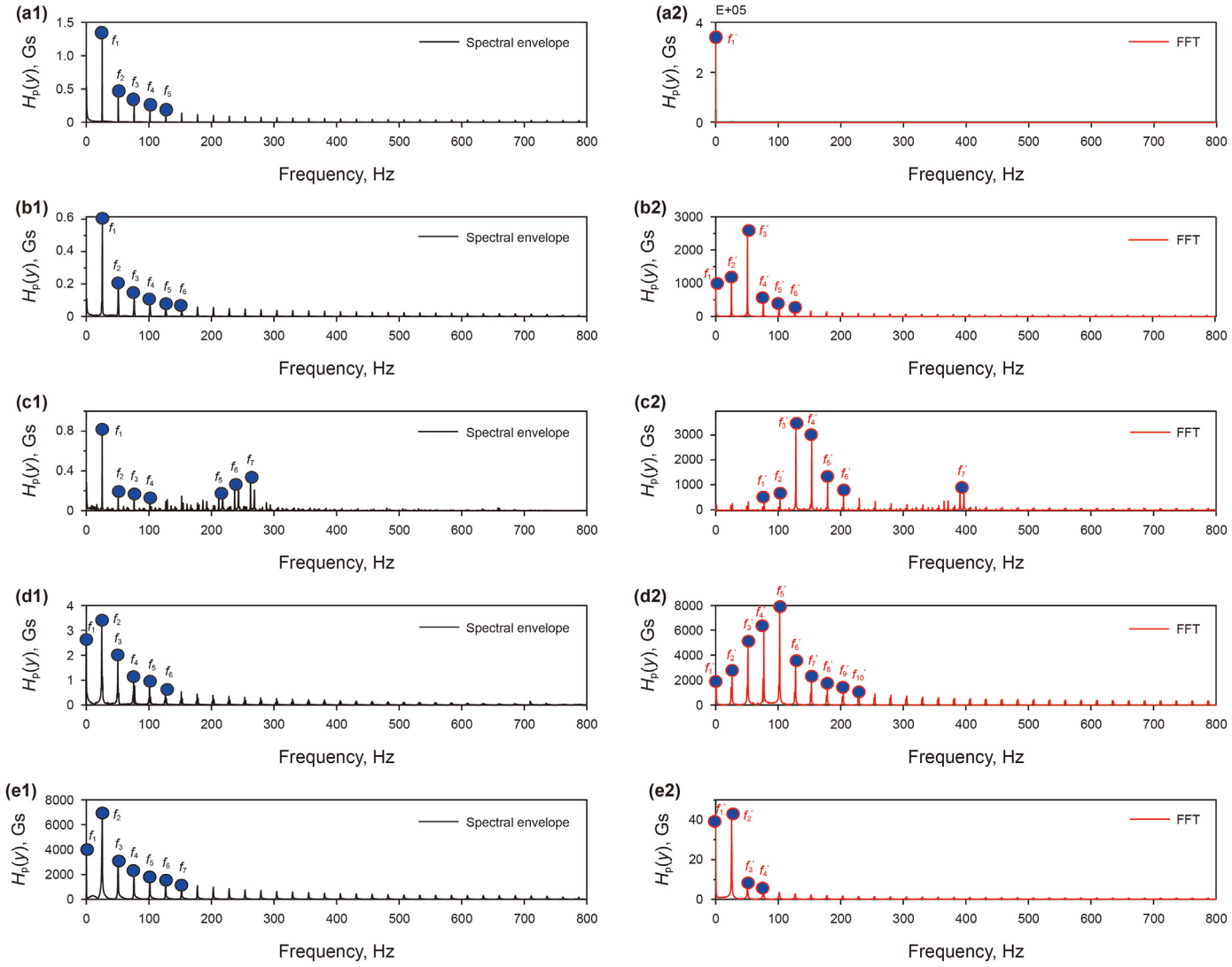

Fig. 19. Frequency domain results of five defects. The black line is the spectral envelope processing result, and the red line is the FFT spectrum processing result. (a-1) Spectral envelope for normal; (a-2) FFT spectrum for normal. (b-1) Spectral envelope for girth-welding position; (b-2) FFT spectrum for girth-welding position. (c-1) Spectral envelope for corrosion at spiral welding position; (c-2) FFT spectrum for corrosion at spiral welding position. (d-1) Spectral envelope for transverse mechanical scratches; (d-2) FFT spectrum for transverse mechanical scratches. (e−1) Spectral envelope for dent; (e−2) FFT spectrum for dent.

Declaration of competing interest

The authors declare that they have no known competing financial interests or personal relationships that could have appeared to influence the work reported in this paper.

Acknowledgments

This work is sponsored by the National Key Research and Development Program of China (No. 2018YFF0215003), State Key Laboratory of Process Automation in Mining & Metallurgy and Beijing Key Laboratory of Process Automation in Mining & Metallurgy (No. BGRIMM-KZSKL- 2021-04), Tribology Science Fund of State Key Laboratory of Tribology (No. SKLTKF20B15).

References

An, X., Pan, L., 2017. Bearing fault diagnosis of a wind turbine based on variational mode decomposition and permutation entropy. Proc. Inst. Mech. Eng. O J. Risk Reliab. 231 (2), 200–206. https://doi.org/10.1177/1748006X17693492, 2017.

Anon, 1998. Natural Gas Pipelines: Greater Use of Instrumented Inspection Technology Can Improve Safety. General Accounting Office, Washington, DC, p. 379. https://doi.org/10.1016/S0963-8695 (98)90871-4 (United States), PB93-113447/GAR, 50pp. (Sep. 1992), NDT & E International, 31(5)(1998).

Atzlesberger, J., Zagar, B., 2010. Magnetic flux leakage measurement set up for defect detection. Procedia Eng. 5, 1401–1404. https://doi.org/10.1016/j.proeng.2010.09.377, 2010.

Buzug, T., Pfister, G., 1992. Optimal delay time and embedding dimension for delay-time coordinates by analysis of the global static and local dynamical behavior of strange attractors. Phys. Rev. 45 (10), 7073. https://doi.org/10.1103/PhysRevA.45.7073, 1992.

Cai, S.C., 2006. Application of EMD in the signal process of pipeline defect magnetic flux leakage inspection. China Mech. Eng. 17 (21), 2201–2203. https://doi.org/10.3321/j.issn:1004-132X.2006.21.001, 2006.

Chaburkin, V.F., 1998. The effect of flaws on serviceability of oil and gas pipeline welds. Proceedings of the 10th International Offshore Mechanics and Arctic Engineering Conference 31 (5). https://doi.org/10.1016/S0963-8695(98)90899-4 (1998), PP. 382-0.

Chen, S.Y., Zhang, Q., Mclellan, B., Zhang, T.T., 2020. Review on the petroleum market in China: history, challenges and prospects. Petrol. Sci. 17 (6), 1779–1794. https://doi.org/10.1007/s12182-020-00501-6, 2020.

Chen, J.J., Huang, S.L., Zhao, W., 2014. Three-dimensional defect inversion from magnetic flux leakage signals using iterative neural network. IET Sci. Meas. Technol. 9 (4), 418–426. https://doi.org/10.1049/iet-smt.2014.0173, 2015.

Chen, L., Li, X.B., Qin, G.X., Lu, Q., 2008. Signal processing of magnetic flux leakage surface flaw inspect in pipeline steel. Russ. J. Nondestr. Test. 44 (12), 859–867. https://doi.org/10.1134/s1061830908120097, 2008.

Coelho, Y.S., Vilela, G., Machado, F., Machado, D.S., 2018. Inspection of defects in petroleum pipelines by magnetic flux leakage measurements. Encontro de Outono da SBF 2018. https://doi.org/10.13140/RG.2.2.23345.12646 (2018), pp. 537–1.

Dragomiretskiy, K., Zosso, D., 2014. Variational mode decomposition. IEEE Trans. Signal Process. 62 (3), 531–544. https://doi.org/10.1109/TSP.2013.2288675, 2013.

Ge, Y.E., Du, L.D., Wang, Z.Y., Zhou, Y., 2020. A multiobjective programming model for comparing existing and potential corridors between the Indian Ocean and China. In: Maritime Transport and Regional Sustainability. Elsevier, pp. 289–309. https://doi.org/10.1016/B978-0-12-819134-7.00018-6, 2020.

Ghazali, M.F., Samta, A.K., 2019. Leakage detection in pipeline using wavelet transform method. Journal of Science and Applied Engineering 2 (1), 29–34. https://doi.org/10.31328/jsae.v2i1.941, 2019.

Ghoni, R., Dollah, M., Sulaiman, A., Ibrahim, F.M., 2014. Defect characterization based on eddy current technique: technical review. Adv. Mech. Eng. 6, 182496. https://doi.org/10.1155/2014/1824, 2014.

Golafshan, R., Sanliturk, K.Y., 2016. SVD and Hankel matrix based de-noising approach for ball bearing fault detection and its assessment using artificial faults. Mech. Syst. Signal Process. 70, 36–50. https://doi.org/10.1016/j.ymssp.2015.08.012, 2016.

Gu, X.T., Zang, X.R., Zhang, Z.Y., Yang, P., Miao, W.Z., Cao, P., Zhao, B., 2022. Reliability analysis of large-diameter high-grade-steel natural gas pipelines under fault action, 2022 Petrol. Sci.. https://doi.org/10.1016/j.petsci.2022.06.017. Available online 24 June 2022.

Han, W.H., Que, P.W., 2006. A modified wavelet transform domain adaptive FIR filtering algorithm for removing the SPN in the MFL data. Measurement 39 (7), 621–627. https://doi.org/10.1016/j.measurement.2006.01.007, 2006.

Huang, L.C., Tao, B., Chen, D.H., Zhang, X., Li, G.F., 2021. Research on pipe crack detection based on image processing algorithm. Int. J. Wireless Mobile Comput. 20 (4), 328–335. https://doi.org/10.1504/IJWMC.2021.117550, 2021.

Jackson, D., Mohanagayathriand, R., Abudhahir, A., 2014. Characterization of defects in Magnetic Flux Leakage (MFL) images using wavelet transform and neural network. In: 2014 International Conference on Electronics and Communication Systems. (ICECS), pp. 1–5, 2014.

Jiang, Y., Bao, X., Hao, S.N., Zhao, H.T., Li, X.Y., Wu, X.N., 2020. Monthly streamflow forecasting using ELM-IPSO based on phase space reconstruction. Water Resour. Manag. 34 (11), 3515–3531. https://doi.org/10.1007/s11269-020-02631-3, 2020.

Kalman, D., 1996. A singularly valuable decomposition: the SVD of a matrix. The college mathematics journal, 1996 27 (1), 2–23. https://doi.org/10.1080/07468342.1996.11973744, 1996.

Kercel, S.W., Tucker, R.W., Varma, V.K., 2003. Pipeline flaw detection with wavelet packets and gas. Proc. SPIE-Int. Soc. Opt. Eng. 5103, 217–226. https://doi.org/10.1117/12.496975, 2003.

Lam, C., Zhou, W., 2016. Statistical analyses of incidents on onshore gas transmission pipelines based on PHMSA database. Int. J. Pres. Ves. Pip. 145, 29–40. https://doi.org/10.1016/j.ijpvp.2016.06.003, 2016.

Li, Y.T., He, X.N., Shuai, J., 2021a. Risk analysis and maintenance decision making of natural gas pipelines with external corrosion based on Bayesian network. Petrol. Sci. 19 (3), 1250–1261. https://doi.org/10.1016/j.petsci.2021.09.016, 2022.

Li, J.M., Yao, X.F., Wang, H., Zhang, J.F., 2019. Periodic impulses extraction based on improved adaptive VMD and sparse code shrinkage denoising and its application in rotating machinery fault diagnosis. Mechanical Systems and Signal Processing, 2019 126 (7), 568–589. https://doi.org/10.1016/j.ymssp.2019.02.056, 2019.

Li, L., Zhang, G.Z., Liu, J.Z., Han, L., Zhang, J.J., 2021b. Estimation of fracture density and orientation from azimuthal elastic impedance difference through singular value decomposition. Petrol. Sci. 18 (6), 1675–1688. https://doi.org/10.1016/j.petsci.2021.09.037, 2021.

Lian, J.J., Liu, Z., Wang, H.J., Dong, X.F., 2018. Adaptive variational mode decomposition method for signal processing based on mode characteristic. Mech. Syst. Signal Process. 107 (7), 53–77. https://doi.org/10.1016/j.ymssp.2018.01.019, 2018.

Liu, Y.T., Tao, B., Jiang, G.Z., Li, G.Z., Zhang, X., Chen, D.H., 2020. Water leakage detection and localisation based on GCC-PHAT algorithm. Int. J. Wireless Mobile Comput. 19 (1), 55–61. https://doi.org/10.1504/IJWMC.2020.109264, 2020.

Liu, T., Chen, J., Dong, G.M., 2015. Singular spectrum analysis and continuous hidden Markov model for rolling element bearing fault diagnosis. Journal of Vibration and Control, 2015 21 (8), 1506–1521. https://doi.org/10.1177/1077546313496833, 2015.

Liu, B., Zeng, Z., Wang, H., 2021. Study on the early fatigue damage evaluation of high strength steel by using three components of metal magnetic memory signal. NDT E Int. 117 (2021), 102380. https://doi.org/10.1016/j.ndteint.2020.102380.

Lu, J.Y., Qu, X., Wang, D.M., Yue, J.K., Zhu, L.J., Li, G.F., 2021. Application of a noise reduction method combining AVMD and SVD in natural gas pipeline leakage signal. Systems Science & Control Engineering 9 (1), 380–392. https://doi.org/10.1080/21642583.2021.1913450, 2021.

Mukherjee, D., Saha, S., Mukhopadhyay, S., 2012. An adaptive channel equalization algorithm for MFL signal. NDT E Int. 45 (1), 111–119. https://doi.org/10.1016/j.ndteint. 2011.08.011, 2012.

Peng, X., Anyaoha, U., Liu, Z., Tsukada, K., 2020. Analysis of magnetic flux leakage (MFL) data for pipeline corrosion assessment. IEEE Trans. Magn. 56 (6), 1–15. https://doi.org/10.1109/TMAG.2020.2981450, 2020.

Shannon, C.E., 1948. A mathematical theory of communication. The Bell system technical journal 27 (3), 379–423. https://doi.org/10.1002/j.1538-7305.1948.tb01338.x, 1948.

Tong, X.G., Zhang, G.Y., Wang, Z.M., Wen, Z.X., Tian, Z.J., Wang, H.J., Ma, F., Wu, Y.P., 2018. Distribution and potential of global oil and gas resources. Petrol. Explor. Dev. 45 (4), 779–789. https://doi.org/10.11698/PED.2018.04.19, 2018.

Vashishtha, G., Kumar, R., 2022. Pelton wheel bucket fault diagnosis using improved SE and expectation maximization principal component analysis. Journal of Vibration Engineering & Technologies 10 (1), 335–349. https://doi.org/10.1007/s42417-021-00379-7, 2022.

Wang, Y.X., Richard, M., Xiang, J.W., Zheng, W.G., 2015. Research on variational mode decomposition and its application in detecting rub-impact fault of the rotor system. Mech. Syst. Signal Process. 60, 243–251. https://doi.org/10.1016/j.ymssp.2015.02.020, 2015.

Wang, D.M., Zhu, L.J., Yue, J.Y., Lu, J.Y., Li, G.F., 2022. Application of improved variational mode decomposition method based on two-dimensional sparrow search algorithm in natural gas pipeline leakage signal denoising. Trans. Inst. Meas. Control 44 (13), 2588–2602. https://doi.org/10.1177/01423312211063688, 2022.

Wang, J., 2015. Fault feature extraction method of rolling bearings based on singular value decomposition and local mean decomposition. J. Mech. Eng. 51 (3), 104. https://doi.org/10.3901/JME.2015.03.104, 2015.

Yang, L.J., Wang, Z.J., Gao, S.W., Shi, M., Liu, B.L., 2019a. Magnetic flux leakage image classification method for pipeline weld based on optimized convolution kernel. Neurocomputing 365, 229–238. https://doi.org/10.1016/j.neucom.2019.07.083, 2019a.

Yang, L.J., Wang, Z.J., Gao, S.W., 2019b. Pipeline magnetic flux leakage image-detection algorithm based on multi-scale SSD network. IEEE Trans. Ind. Inf. 16 (1), 501–509. https://doi.org/10.1109/TII.2019.2926283, 2019.

Yol, S., Ozdemir, M.A., Akan, A., Chaparro, L.F., 2018. Detection of epileptic seizures by the analysis of EEG signals using empirical mode decomposition. In: 2018 Medical Technologies National Congress (TIPTEKNO). IEEE, pp. 1–4. https://doi.org/10.1109/TIPTEKNO.2018.8596780, 2018.

Zhao, X.Z., Ye, B.Y., 2009. Similarity of signal processing effect between Hankel matrix-based SVD and wavelet transform and its mechanism analysis. Mech. Syst. Signal Process. 23 (4), 1062–1075. https://doi.org/10.1016/j.ymssp.2008.09.009, 2009.

Zhou, Y.N., Zhang, Y., Lu, J.Y., Yang, F., Dong, H.L., Li, G.F., 2022. Feature extraction method of pipeline signal based on parameter optimized vocational mode decomposition and exponential entropy. Trans. Inst. Meas. Control 44 (1), 216–231. https://doi.org/10.1177/01423312211029440, 2022.